

# Catalyzing Generation and Stabilization of Oxygen Vacancies on $\text{CeO}_{2-x}$ Nanorods by Pt Nanoclusters as Nanozymes for Catalytic Therapy

Jiankang Zhang, Yu Yang, Fengmin Qin, Tingting Hu, Xinshuo Zhao, Shichao Zhao, Yueqiang Cao, Zhe Gao, Zhan Zhou,\* Ruizheng Liang,\* Chaoliang Tan,\* and Yong Qin

Although  $\text{CeO}_2$  nanomaterials have been widely explored as nanozymes for catalytic therapy, they still suffer from relatively low activities. Herein, the catalyzing generation and stabilization of oxygen vacancies on  $\text{CeO}_2$  nanorods by Pt nanoclusters via  $\text{H}_2$  gas reduction under mild temperature (350 °C) to obtain  $\text{Pt/CeO}_{2-x}$ , which can serve as a highly efficient nanozyme for catalytic cancer therapy, is reported. The deposited Pt on  $\text{CeO}_2$  by the atomic layer deposition technique not only can serve as the catalyst to generate oxygen vacancies under mild temperature reduction through the hydrogen spillover effect, but also can stabilize the generated oxygen vacancies. Meanwhile, the oxygen vacancies also provide anchoring sites for Pt forming strong metal-support interactions and thus preventing their agglomerations. Importantly, the  $\text{Pt/CeO}_{2-x}$  reduced at 350 °C ( $\text{Pt/CeO}_{2-x}$ -350R) exhibits excellent enzyme-mimicking catalytic activity for generation of reactive oxygen species (e.g.,  $\cdot\text{OH}$ ) as compared to other control samples, including  $\text{CeO}_2$ ,  $\text{Pt/CeO}_2$ , and  $\text{Pt/CeO}_{2-x}$  reduced at other temperatures, thus achieving excellent performance for tumor-specific catalytic therapy to efficiently eliminate cancer cells in vitro and ablate tumors in vivo. The excellent enzyme-mimicking catalytic activity of  $\text{Pt/CeO}_{2-x}$ -350R originates from the good catalytic activities of oxygen vacancy-rich  $\text{CeO}_{2-x}$  and Pt nanoclusters.

## 1. Introduction

Catalytic therapy is a new type of tumor treatment method developed in recent years since it can respond to the tumor microenvironment (TME) to produce reactive oxygen species (ROS) and can effectively remove deep tumors in the tissues.<sup>[1–11]</sup> Developing highly effective nanozymes has been as of the key issues in the field of catalytic therapy.<sup>[12–19]</sup> Since  $\text{Fe}_3\text{O}_4$  nanoparticles were first reported to exhibit activity similar to that of natural horseradish peroxidase in 2007,<sup>[20]</sup> various nanomaterials have been designed and developed as nanozymes, including noble metals (e.g., Pt, Au, and Pd), metal oxides (e.g.,  $\text{MnO}_2$ ,  $\text{MoO}_3$ ,  $\text{WO}_3$ ,  $\text{Co}_3\text{O}_4$ ,  $\text{Cu}_2\text{O}$ , and  $\text{CeO}_2$ ), layered double hydroxides (LDHs), carbon nanomaterials, and transition metal chalcogenides (e.g.,  $\text{MoS}_2$ ,  $\text{FeS}_2$ , and  $\text{MoSe}_2$ ).<sup>[21–35]</sup> Among them, metal oxides have received considerable attention as nanozymes for catalytic therapy due to their easy preparation and modification,

J. Zhang, F. Qin, Y. Qin  
Interdisciplinary Research Center of Biology and Catalysis  
School of Life Sciences  
Northwestern Polytechnical University  
Xi'an 710072, P. R. China

Y. Yang, T. Hu, R. Liang  
State Key Laboratory of Chemical Resource Engineering  
Beijing Advanced Innovation Center for Soft Matter Science and Engineering  
Beijing University of Chemical Technology  
Beijing 100029, P. R. China  
E-mail: liangrz@mail.buct.edu.cn


X. Zhao, Z. Zhou  
College of Chemistry and Chemical Engineering  
Henan Key Laboratory of Function-Oriented Porous Materials  
Luoyang Normal University  
Luoyang 471934, P. R. China  
E-mail: zhouzhan@lynu.edu.cn

S. Zhao, Z. Gao, Y. Qin  
State Key Laboratory of Coal Conversion  
Institute of Coal Chemistry  
Chinese Academy of Sciences  
Taiyuan 030001, P. R. China

Y. Cao  
State Key Laboratory of Chemical Engineering  
School of Chemical Engineering  
East China University of Science and Technology  
Shanghai 200237, P. R. China

C. Tan  
Department Electrical and Electronic Engineering  
The University of Hong Kong  
Pokfulam Road, Hong Kong, SAR 999077, P. R. China  
E-mail: cltan@hku.hk

R. Liang  
Quzhou Institute for Innovation in Resource Chemical Engineering  
Quzhou 324000, P. R. China

 The ORCID identification number(s) for the author(s) of this article can be found under <https://doi.org/10.1002/adhm.202302056>

© 2023 The Authors. Advanced Healthcare Materials published by Wiley-VCH GmbH. This is an open access article under the terms of the Creative Commons Attribution-NonCommercial License, which permits use, distribution and reproduction in any medium, provided the original work is properly cited and is not used for commercial purposes.

DOI: 10.1002/adhm.202302056

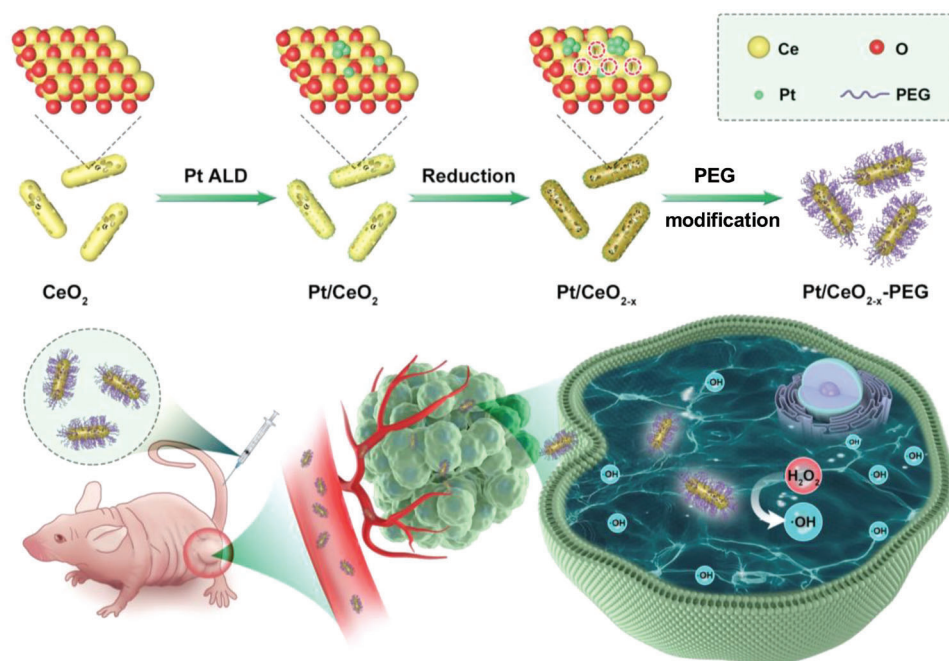


**Figure 1.** Schematic illustration of the synthesis of Pt/CeO<sub>2-x</sub> nanozymes and their surface modifications with PEG for catalytic therapy.

tunable performance, excellent biocompatibility, and biodegradability. For example, Zhang et al. reported a novel Janus-like Fe@Fe<sub>3</sub>O<sub>4</sub>-Cu<sub>2</sub>O heterostructure as the enzyme catalytic agent for endogenous long-acting catalytic therapy.<sup>[36]</sup> Recently, CeO<sub>2</sub> nanomaterials have been demonstrated to display great potential as nanozymes owing to their tunable electronic property (Ce<sup>4+</sup>/Ce<sup>3+</sup>) and oxygen vacancy, low biotoxicity, excellent biocompatibility, and multienzyme activity.<sup>[37–42]</sup> However, the catalytic activities of previously reported CeO<sub>2</sub> nanomaterials are quite poor, which greatly limits their further applications as nanozymes in catalytic therapy.

Defect engineering, such as generation of oxygen vacancies, has been proven to be a simple but powerful strategy to optimize or significantly enhance the catalytic activity of metal oxide/hydroxide nanomaterials (e.g., MoO<sub>3</sub>, WO<sub>3</sub>, TiO<sub>2</sub>, MnO<sub>2</sub>, and CeO<sub>2</sub>) in catalysis field since the introduced oxygen vacancies can significantly tune their electronic structures and optimize the activities of their active sites.<sup>[43–49]</sup> Importantly, defect engineering has also been demonstrated to be a promising approach to activate/optimize the performance of metal oxide/hydroxide nanomaterials for biomedical applications such as photodynamic therapy, sonodynamic therapy, and catalytic therapy in last few years.<sup>[50–55]</sup> As a typical example, we have first reported the significant boosting the photodynamic therapy performance of 2D LDH nanosheets by defect engineering induced by simple acidic etching,<sup>[52]</sup> which was further extended to sonodynamic therapy in a later study.<sup>[53]</sup> Elemental doping or guest intercalation has also been developed as effective ways to induce rich defect engineering on layered MoO<sub>3</sub>, thus significantly improving their performance when used as nanozymes in catalytic therapy.<sup>[54,55]</sup> Promisingly, recent studies have demonstrated that defect engineering is an effective strategy to boost the enzyme-like catalytic activities of CeO<sub>2</sub> nanomaterials for catalytic cancer therapy. It

was found that transition metal (e.g., Mn/Zr and Fe) doping can generate rich defects on CeO<sub>2</sub> nanocrystals and promote their enzyme-like catalytic activities for ROS generation, thus achieving good performance in catalytic cancer therapy.<sup>[56,57]</sup> However, the currently reported doped CeO<sub>2</sub>-based nanozymes still suffer from relatively low catalytic activity or need to assist by photothermal effect and/or introduce additional active metal elements like Mn or Fe.

Herein, we report a simple and powerful strategy to develop highly efficient nanozymes based on CeO<sub>2</sub> nanorods (NRs) supported high-dispersion Pt nanoclusters. Pt nanoclusters were deposited on the hydrothermal-synthesized porous CeO<sub>2</sub> NRs by atomic layer deposition (ALD) process, an advanced technique for the synthesis of nanomaterials with specific structures and functions,<sup>[58,59]</sup> to prepare Pt/CeO<sub>2</sub>, which was then reduced by H<sub>2</sub> gas under different temperatures (from 30 to 650 °C) to obtain the oxygen vacancy-rich Pt/CeO<sub>2-x</sub> (**Figure 1**). Importantly, the deposited Pt nanoclusters not only can serve as the catalyst to generate oxygen vacancies at mild temperature or even room temperature reduction by hydrogen spillover effect, but also can stabilize the generated oxygen vacancies. Meanwhile, the oxygen vacancies also provide the anchoring sites for Pt nanoclusters forming strong metal-support interactions and thus preventing their agglomerations. The Pt/CeO<sub>2-x</sub> reduced at 350 °C (Pt/CeO<sub>2-x</sub>-350R) exhibits the optimized enzyme-mimicking catalytic activity among the synthesized samples. Thus, after modification with polyethylene glycol, the Pt/CeO<sub>2-x</sub>-350R can be used as highly efficient nanozyme for catalytic therapy to efficiently kill cancer cells in vitro and eliminate tumors in vivo. Both the good catalytic activities of oxygen vacancy-rich CeO<sub>2-x</sub> and Pt nanoclusters contribute to the boosted enzyme-mimicking catalytic activity of Pt/CeO<sub>2-x</sub>-350R, which may be further enhanced by the synergistic effect between them.

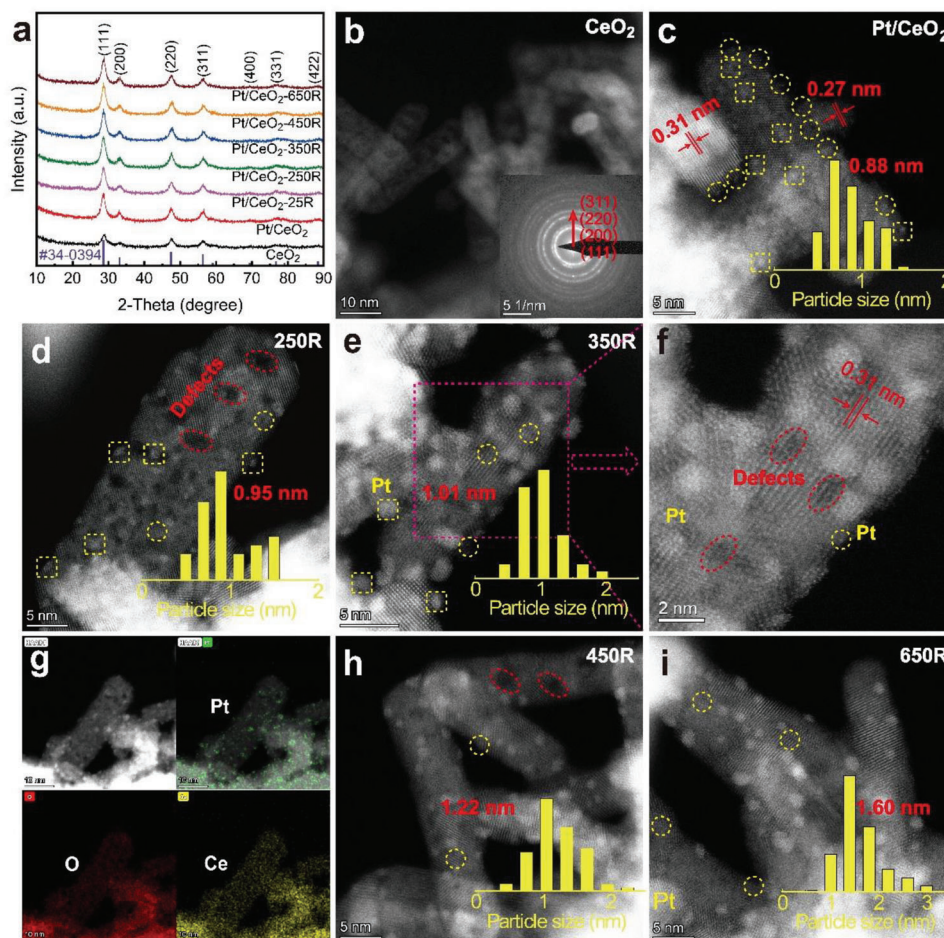


**Figure 2.** Structure and micromorphology of the materials. a) XRD patterns of the materials. HAADF-STEM images of the as-prepared b)  $\text{CeO}_2$  (Inset is SAED), c)  $\text{Pt/CeO}_2$ , activated d)  $\text{Pt/CeO}_{2-x}$ -250R, e,f)  $\text{Pt/CeO}_{2-x}$ -350R, h)  $\text{Pt/CeO}_{2-x}$ -450R, and i)  $\text{Pt/CeO}_{2-x}$ -650R. g) Elemental mapping images of the  $\text{Pt/CeO}_{2-x}$ -350R. Insets in (c–i) are the corresponding histograms of PSD of the corresponding materials.

## 2. Results and Discussion

### 2.1. Synthesis, Characterization, and DFT Calculation of $\text{Pt/CeO}_2$ and $\text{Pt/CeO}_{2-x}$

The porous  $\text{CeO}_2$  NRs were first synthesized by a slightly modified two-step solvothermal synthesis approach (see details in Section S1, Supporting Information).<sup>[60]</sup> As shown in **Figure 2a**, all the peaks in the X-ray diffraction (XRD) pattern of the  $\text{CeO}_2$  NRs match well with the fluorite phase  $\text{CeO}_2$  (PDF-#34-0394), confirming its crystal structure. As evidenced by the aberration-corrected high-angle annular dark-field scanning transmission electron microscopy (HAADF-STEM) image (**Figure 2b**), the obtained  $\text{CeO}_2$  sample has a nanorod morphology with a length of  $\approx 52$  nm and diameter of  $\approx 5.5$  nm with rich nano-sized pores (**Figure S1**, Supporting Information). The selected area electron diffraction (SAED) pattern demonstrates the polycrystalline nature of the synthesized  $\text{CeO}_2$  NRs (inset in **Figure 2b**). Then, highly dispersed Pt species were deposited on the surface of  $\text{CeO}_2$  NRs by ALD technique to obtain the as-prepared  $\text{Pt/CeO}_2$  sample. The XRD pattern of the  $\text{Pt/CeO}_2$  matches well with that of  $\text{CeO}_2$  NRs since the deposited Pt species are too small to give ob-

vious XRD peaks (**Figure 2a**). As shown in **Figure 2c**, the HAADF-STEM image of the as-prepared  $\text{Pt/CeO}_2$  (1.13 wt% of Pt) shows that the Pt nanoclusters (labeled by yellow squares) with an average particle size (APS) of 0.88 nm (inset in **Figure 2c**) along with Pt single atoms (SAs: labeled by yellow circles) are highly dispersed on the  $\text{CeO}_2$  NRs. It was found that part of the nanoclusters is composed of randomly assembled Pt atoms (nearly atomic clusters), exhibiting atomically dispersed features. The measured lattice spacings of  $\text{CeO}_2$  are 0.31 and 0.27 nm (**Figure 2c**), which correspond to the (111) and (200) planes of  $\text{CeO}_2$  crystal, respectively.<sup>[61]</sup> The  $\text{N}_2$  adsorption–desorption results show that the deposition of Pt species results in the decrease of the specific surface area from 124 to 103  $\text{m}^2 \text{g}^{-1}$  and pore volume from 0.5 to 0.4  $\text{cm}^3$  of the  $\text{CeO}_2$  NRs (**Figure S2**, Supporting Information), suggesting that Pt species might be also deposited in the pores of  $\text{CeO}_2$  NRs. The  $\text{Pt/CeO}_2$  sample is further reduced at different temperatures by  $\text{H}_2$  gas to obtain a few  $\text{Pt/CeO}_{2-x}$  samples and those samples are denoted as  $\text{Pt/CeO}_{2-x}$ -30R (reduced at 30 °C),  $\text{Pt/CeO}_{2-x}$ -250R (reduced at 250 °C),  $\text{Pt/CeO}_{2-x}$ -350R (reduced at 350 °C),  $\text{Pt/CeO}_{2-x}$ -450R (reduced at 450 °C), and  $\text{Pt/CeO}_{2-x}$ -650R (reduced at 650 °C) based on their reduction temperatures. The XRD diffraction peaks of all reduced samples match

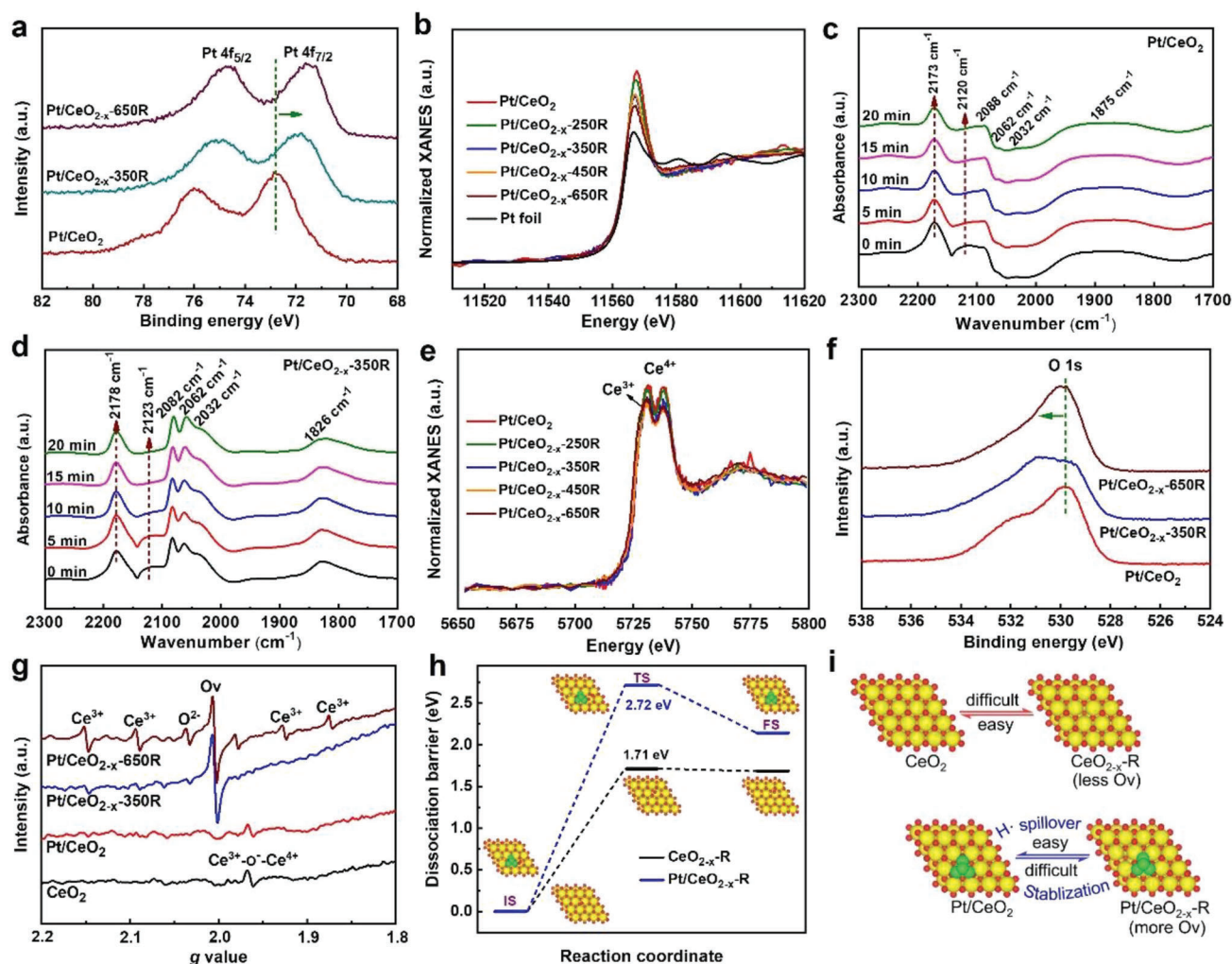


**Figure 3.** Physicochemical properties of the materials. a) XPS Pt 4f spectra of Pt/CeO<sub>2</sub>, Pt/CeO<sub>2-x</sub>-350R, and Pt/CeO<sub>2-x</sub>-650R. b) Normalized Pt L3-edge XANES spectra of Pt/CeO<sub>2</sub>, Pt/CeO<sub>2-x</sub>-250R, Pt/CeO<sub>2-x</sub>-350R, Pt/CeO<sub>2-x</sub>-450R, Pt/CeO<sub>2-x</sub>-650R, and Pt foil. In situ CO-DRIFTS spectra of c) Pt/CeO<sub>2</sub> and d) Pt/CeO<sub>2-x</sub>-350R. e) Normalized Ce L3-edge XANES spectra of Pt/CeO<sub>2</sub>, Pt/CeO<sub>2-x</sub>-250R, Pt/CeO<sub>2-x</sub>-350R, Pt/CeO<sub>2-x</sub>-450R, Pt/CeO<sub>2-x</sub>-650R, and Pt foil. f) XPS O 1s spectra of Pt/CeO<sub>2</sub>, Pt/CeO<sub>2-x</sub>-350R, and Pt/CeO<sub>2-x</sub>-650R. g) EPR spectra of CeO<sub>2</sub>, Pt/CeO<sub>2</sub>, Pt/CeO<sub>2-x</sub>-350R, and Pt/CeO<sub>2-x</sub>-650R. h) Comparison of O<sub>2</sub> dissociation barrier over the two reduced nanozymes (IS, TS, and FS represent initial state, transition state, and final state, respectively). i) Schematic illustration of the redox properties of CeO<sub>2</sub>, CeO<sub>2</sub>-R, Pt/CeO<sub>2</sub>, and Pt/CeO<sub>2-x</sub>-R.

well with that of the Pt/CeO<sub>2</sub> (Figure 2a). For Pt/CeO<sub>2-x</sub>-250R, the APS of Pt nanoclusters only slightly increases ( $\approx 0.95$  nm, Figure 2d; Figure S3, Supporting Information) compared with that of the as-prepared Pt/CeO<sub>2</sub> sample. Similar result is also observed for the Pt/CeO<sub>2-x</sub>-350R, whose APS of Pt nanoclusters increases to  $\approx 1.01$  nm (Figure 2e,f). Further characterization by energy-dispersive X-ray spectroscopy mapping (Figure 2g) confirms the uniform distribution of the Pt on the CeO<sub>2</sub> NRs. Although the corresponding Pt APS increases to  $\approx 1.22$  and  $1.60$  nm for the Pt/CeO<sub>2-x</sub>-450R (Figure 2h; Figure S4, Supporting Information) and Pt/CeO<sub>2-x</sub>-650R (Figure 2i; Figure S5, Supporting Information), respectively, there still exist some SAs on the CeO<sub>2-x</sub> surface.

In addition to the particle size, the reduction process also remarkably changes the electronic properties of the Pt. From the X-ray photoelectron spectroscopy (XPS) survey spectra (Figure S6,

Supporting Information), Pt, O, and Ce are all detected, again indicating the successful Pt deposition on CeO<sub>2</sub>. As also can be seen from the Pt 4f spectra, the Pt 4f binding energy monotonously shifts to lower positions with the increased reduction temperature (Figure 3a). Such result suggests that Pt is negatively charged (electron-rich state) and changes to lower valence state after the reduction process. This can be further verified by the X-ray absorption fine structure spectroscopy characterization. Figure 3b shows the Pt L<sub>3</sub> X-ray absorption near edge structure (XANES) spectra of Pt/CeO<sub>2</sub>, Pt/CeO<sub>2-x</sub>-250R, Pt/CeO<sub>2-x</sub>-350R, Pt/CeO<sub>2-x</sub>-450R, Pt/CeO<sub>2-x</sub>-650R, and Pt foil, and the white-line intensity decreases monotonously with increased reduction temperature, indicating the gradually decreased valence states. To further determine the electronic structure changes of Pt after reduction, the Pt/CeO<sub>2</sub> and Pt/CeO<sub>2-x</sub>-350R samples were tested by the diffuse reflectance infrared Fourier transform

spectroscopy of CO adsorption (CO-DRIFTS). As shown in the curves of Pt/CeO<sub>2</sub> (Figure 3c), the bands at around 2173 and 2120 cm<sup>-1</sup> are the gas-phase CO molecule vibrations, and the latter band gradually disappears with increased purge time.<sup>[62,63]</sup> There also exist three weak bands at around 2088, 2062, and 2032 cm<sup>-1</sup> in the spectrum of as-prepared Pt/CeO<sub>2</sub> (Figure 3c), which should be assigned to CO molecules adsorbed at atomic Pt<sup>δ+</sup>, edge and/or corner sites of low-coordination Pt clusters, and electron-rich Pt nanoclusters.<sup>[64]</sup> Additionally, the broad band at around 1875 cm<sup>-1</sup> assigned to bridge-bonded CO also indicates the existence of partial Pt nanoparticles in Pt/CeO<sub>2</sub>.<sup>[62,63]</sup> Similar case is found from the spectrum of reduced Pt/CeO<sub>2-x</sub>-350R except that the bands become sharper and the bridge-bonded band shifts to the lower wavenumber (Figure 3d), suggesting that the Pt species are not obviously changed under the low reduction temperature, which are consistent with the aforementioned HAADF-STEM results (Figure 2e). Nevertheless, obvious changes can be found from the spectrum of Pt/CeO<sub>2-x</sub>-650R compared with the other two counterparts. The two bands of CO molecule vibrations almost disappear with increased purge time, and a new narrow band at around 2078 cm<sup>-1</sup> accompanied with a weak band at around 2021 cm<sup>-1</sup> (Figure S7, Supporting Information), strongly proving the reconstruction of Pt species at the higher reduction temperature.

Interestingly, the color of Pt/CeO<sub>2</sub> significantly changes during the reduction process. As shown in Figure S8, Supporting Information, the color of Pt/CeO<sub>2</sub> changes from light yellow to brown even reduced at room temperature, and it gradually deepens to dark brown as the reduction temperature increases from 30 to 650 °C. It is worth pointing out that the Pt/CeO<sub>2-x</sub>-350R yields a much darker color than that of CeO<sub>2-x</sub>-350R under the same conditions, that is, reduction at 350 °C (Figure S8, Supporting Information). Such result clearly suggests that the presence of Pt species could promote the reduction of CeO<sub>2</sub> by H<sub>2</sub> gas. Note that the Pt/CeO<sub>2</sub> can even be reduced by H<sub>2</sub> at room temperature. As shown in Figure S9, Supporting Information, the color of the sample gradually changes from brown to dark brown after reduced around 25 min by H<sub>2</sub> at 30 °C. In contrast, the bare CeO<sub>2</sub> NRs cannot be reduced at 30 °C under the same condition (Figure S10, Supporting Information), further indicating the promoted reduction of CeO<sub>2</sub> by Pt species. However, the color of the reduced Pt/CeO<sub>2-x</sub>-30R will change back in few minutes in air after taking out from the tube-furnace (Figure S10, Supporting Information). Color changes normally indicate the absorption changes of the samples. Therefore, all the samples were characterized by the ultraviolet-visible (UV-vis) diffuse reflectance spectra. As shown in Figure S11, Supporting Information, the prepared CeO<sub>2</sub> NRs present a strong and broad absorption band in the UV-vis region (from 200 to 500 nm), while showing almost no absorption in the near-infrared region (beyond 800 nm). After depositing Pt nanoclusters/SAs, the Pt/CeO<sub>2</sub> exhibits a decent absorption in the near-infrared region as well as UV-vis region. The relative absorption intensity of the Pt/CeO<sub>2-x</sub> samples in the near-infrared region continues to increase as the reduction temperature increases. According to previous literature,<sup>[65–67]</sup> the reduction of CeO<sub>2</sub> by H<sub>2</sub> normally will generate rich oxygen vacancies and induce partial reduction of Ce<sup>4+</sup> to lower valence state. To explore the structural changes of the CeO<sub>2</sub> during the reduction process, the samples were characterized by various

techniques. As shown in Figure 3e, the normalized Ce L<sub>3</sub>-edge XANES spectra of Pt/CeO<sub>2</sub>, Pt/CeO<sub>2-x</sub>-250R, Pt/CeO<sub>2-x</sub>-350R, Pt/CeO<sub>2-x</sub>-450R, and Pt/CeO<sub>2-x</sub>-650R show that the intensity of the line diminishes consistently with the increase of reduction temperature, suggesting a gradual reduction in valence states of the Ce element. Figure 3f presents that the O 1s binding energy shifts to higher positions with the increased reduction temperature, further proving the presence of oxygen vacancies caused by reduction. As shown in the electron paramagnetic resonance (EPR) spectra (Figure 3g), the peak at around  $g = 2.004$  can be readily assigned to the oxygen vacancy.<sup>[68]</sup> It was found that the peak for oxygen vacancy is quite low for the CeO<sub>2</sub> and Pt/CeO<sub>2</sub> samples and the Ce<sup>3+</sup>-O-Ce<sup>4+</sup> defect peaks are both detected from them.<sup>[69,70]</sup> However, the peaks disappear after the reduction treatment. As expected, both the Pt/CeO<sub>2-x</sub>-350R and Pt/CeO<sub>2-x</sub>-650R show a much stronger peak for oxygen vacancies. All the aforementioned results suggest that rich oxygen vacancies can be generated on the CeO<sub>2</sub> NRs by H<sub>2</sub> and the Pt species can facilitate the generation of oxygen vacancies by serving as the catalyst.

Based on all the aforementioned analysis, it is concluded that the reduction of Pt/CeO<sub>2</sub> by H<sub>2</sub> at mild temperature (e.g., 350 °C) can induce structural changes both on Pt species and CeO<sub>2</sub>. As for Pt, the reduction treatment not only can induce the APS increase slightly, but also can lower its valence state. As for the CeO<sub>2</sub>, the reduction treatment not only can generate rich oxygen vacancies on CeO<sub>2</sub> to obtain CeO<sub>2-x</sub>, but also can partially reduce Ce<sup>4+</sup> to lower valence state. Importantly, the Pt species on the CeO<sub>2</sub> surface can serve as the catalyst to facilitate the reduction of CeO<sub>2</sub> NRs. As we discussed above, the Pt/CeO<sub>2</sub> can even be reduced at room temperature (30 °C) by H<sub>2</sub> because of the catalytic capability of Pt (color change from light brown to dark brown), while the bare CeO<sub>2</sub> NRs is unable to be reduced at the same condition (no color change). Moreover, the Pt/CeO<sub>2</sub> gives rise to a much darker color as compared to the bare CeO<sub>2</sub> NRs when reduced at 350 °C, further proving the catalyzing function of Pt during the reduction process. More importantly, the Pt nanoclusters can also stabilize the mild-temperature generated oxygen vacancies on CeO<sub>2-x</sub> surface. Although previous studies have explored the reduction of CeO<sub>2</sub> nanomaterials by H<sub>2</sub> under annealing, the generated oxygen vacancies only can be stabilized at high reduction temperature (e.g., ~750 °C).<sup>[68]</sup> In our case, the color of the Pt/CeO<sub>2-x</sub>-350R can well retain for long time without obvious change, revealing the stabilization of oxygen vacancies of CeO<sub>2-x</sub> by Pt species under mild reduction temperature (e.g., ~350 °C). Our results prove that the presence of Pt species allows for catalyzing generation and stabilization of rich oxygen vacancies on the surface of CeO<sub>2</sub> NRs under mild reduction temperature.

To explore the mechanism of Pt clusters catalyzing and stabilizing oxygen vacancies on CeO<sub>2</sub>, the as-prepared CeO<sub>2</sub>, and Pt/CeO<sub>2</sub> were further characterized by the H<sub>2</sub>-temperature programmed reduction (H<sub>2</sub>-TPR) profiles under different temperatures (Figure S12, Supporting Information). From the profile of bare CeO<sub>2</sub>, there are two main and one weak hydrogen consumption peaks at around 405, 568, and 728 °C, respectively, which could be assigned to the reduction of sub-/surface oxygen, surface CeO<sub>2</sub> species, and bulk CeO<sub>2</sub>, respectively.<sup>[65–67]</sup> However, the three former peaks disappear, a narrow peak at around 392 °C

and another weak peak at around 122 °C can be observed from the profile of the Pt/CeO<sub>2</sub>. The latter low temperature peak can be ascribed to the reduction of the Pt—O—Ce structure.<sup>[65–67]</sup> The H<sub>2</sub>-TPR result indicates that CeO<sub>2</sub> can be partially reduced in the presence of Pt at a much lower temperature, which is due to the strong hydrogen dissociation and spillover effect from Pt to CeO<sub>2</sub> accompanied with the formation of more oxygen vacancies (Ce<sup>4+</sup> → Ce<sup>3+</sup> + oxygen vacancy).<sup>[71–73]</sup> Therefore, we believe that the size of Pt deposited on the surface of CeO<sub>2</sub> increases with temperature during the reduction process, and it is easier to dissociate hydrogen gas under the action of hydrogen overflow, which catalyzes and stabilizes the oxygen vacancies of CeO<sub>2</sub>. Therefore, the CeO<sub>2</sub> can be reduced at low-temperature to obtain the high active and stable Pt/CeO<sub>2-x</sub>.

Note that the reduced CeO<sub>2-x</sub> species with abundant oxygen vacancies are highly active and unstable, which is easy to be oxidized again once it is exposed to air. The deposition of Pt species can stabilize the formed oxygen vacancies on surface of CeO<sub>2-x</sub> NRs. To further verify this, the antioxidant capacity of reduced CeO<sub>2-x</sub>-R and Pt/CeO<sub>2-x</sub>-R was also calculated based on the density functional theory (DFT) by comparing the O<sub>2</sub> dissociation barrier over the two reduced nanozymes. The result show that O<sub>2</sub> dissociation barrier over Pt/CeO<sub>2-x</sub>-R is 2.72 eV (Figure 3h), which is much higher than that of over CeO<sub>2-x</sub>-R (1.71 eV), suggesting that Pt/CeO<sub>2-x</sub>-R possesses stronger antioxidant capacity. This result indicates that the decoration of Pt clusters on CeO<sub>2-x</sub> can not only promote the formation of oxygen vacancies by the strong hydrogen dissociation and spillover capability (Figure 3i), but also can stabilize the formed oxygen vacancies by resisting oxidation by air. Conversely, oxygen vacancies can also stabilize the Pt by strong metal-support interactions preventing their agglomerations.<sup>[71,74]</sup>

## 2.2. Catalytic Properties Pt/CeO<sub>2</sub> and Pt/CeO<sub>2-x</sub> for ROS Generation and Enhancement Mechanisms

Since both the oxygen vacancy-rich CeO<sub>2-x</sub> and Pt nanoclusters are highly active nanozymes, the Pt/CeO<sub>2-x</sub> is expected to present excellent enzyme-like catalytic activity for ROS generation. To this end, the peroxidase-like activity of CeO<sub>2</sub>, Pt/CeO<sub>2</sub>, and Pt/CeO<sub>2-x</sub> was first assayed in the typical H<sub>2</sub>O<sub>2</sub>-3,3',5,5'-tetramethylbenzidine (TMB) catalytic systems, which can be oxidized by ·OH to form oxidized-TMB (ox-TMB) with characteristic absorbance at 652 nm.<sup>[75,76]</sup> The ·OH generation efficiency mediated by the Fenton reaction determines the catalytic performance. Therefore, we monitored the ·OH generation efficiency of the representative CeO<sub>2</sub>, Pt/CeO<sub>2</sub>, and Pt/CeO<sub>2-x</sub> using TMB (Figure 4a; Figure S13, Supporting Information). The negligible absorbance was observed in CeO<sub>2</sub> group (Figure S13a, Supporting Information), while the absorbance in Pt/CeO<sub>2-x</sub>-350R group demonstrated the most significant enhancement with time (Figure 4a; Figure S13, Supporting Information), approximately twice as that in Pt/CeO<sub>2</sub> group (inset of Figure 4a), suggesting that the optimized Pt/CeO<sub>2-x</sub>-350R exhibits an amazing ·OH production capacity. The generated ·OH was further detected using terephthalic acid (TA). Figure 4b indicated the fluorescence intensity of TA in CeO<sub>2</sub>, Pt/CeO<sub>2</sub>, and Pt/CeO<sub>2-x</sub>-

350R solutions, in which Pt/CeO<sub>2-x</sub>-350R produced the most ROS, as evidenced by the higher fluorescence intensity of TAOH at 432 nm. Moreover, EPR spectroscopy was employed to further validate the generation of ·OH using 5,5-dimethyl-1-pyrroline N-oxide (DMPO) as the specific spin trap reagent. Particularly, stronger ·OH signal can be detected at Pt/CeO<sub>2-x</sub>-350R group compared with Pt/CeO<sub>2</sub> and CeO<sub>2</sub> groups (Figure 4c), which is consistent with the TMB and TA results. The suitable oxygen vacancy concentration, Pt particle size, and physical parameters of Pt/CeO<sub>2-x</sub>-350R lead to its optimized catalytic performance. Besides, the kinetic parameters were also determined via TMB assay by changing the H<sub>2</sub>O<sub>2</sub> concentration at Pt/CeO<sub>2-x</sub>-350R concentration of 100 µg mL<sup>-1</sup> (Figure S14, Supporting Information). The V<sub>max</sub> and K<sub>m</sub> of Pt/CeO<sub>2-x</sub>-350R are calculated to be 2.95 × 10<sup>-6</sup> M s<sup>-1</sup> and 0.45 mM (Figure 4d,e), respectively. Compared with the other reported nanomaterials (Table S1, Supporting Information), Pt/CeO<sub>2-x</sub>-350R presented higher V<sub>max</sub> and lower K<sub>m</sub>, proving its excellent catalytic efficiency.

To further explore the high peroxidase-like catalytic mechanism of Pt/CeO<sub>2-x</sub>-350R and gain deep insights into the synergistic catalytic mechanism between Pt nanoclusters and oxygen vacancies, DFT calculations were used to calculate the free energy of CeO<sub>2</sub>, Pt/CeO<sub>2</sub> and Pt/CeO<sub>2-x</sub>-R. Figure 4f is the free-energy profiles for the peroxidase-like reactions and the corresponding configuration can be found in Figure S15, Supporting Information. The dissociation of H<sub>2</sub>O<sub>2</sub> entity into 2OH\* intermediate on bare CeO<sub>2</sub> is an uphill process (also the rate determining step, RDS, Figure 4f), indicating the poor activating capability of bare CeO<sub>2</sub> toward H<sub>2</sub>O<sub>2</sub>. Even if H<sub>2</sub>O<sub>2</sub> dissociation on bare CeO<sub>2</sub> is thermodynamically possible in whole, it is confronted with a higher activation barrier (0.90 eV). By contrast, the dissociations of H<sub>2</sub>O<sub>2</sub> on both Pt/CeO<sub>2</sub> and activated Pt/CeO<sub>2-x</sub>-R are the dramatic downhill processes, which is especially true for Pt/CeO<sub>2-x</sub>-R. The free energies were calculated to be -3.99 and -4.90 eV for Pt/CeO<sub>2</sub> and Pt/CeO<sub>2-x</sub>-R nanozymes, respectively, suggesting that H<sub>2</sub>O<sub>2</sub> molecule is readily adsorbed and dissociated on the constructed Pt-CeO<sub>2</sub> interfacial sites, which activate this reaction spontaneously from the thermodynamic viewpoint. Note that the dissociation of H<sub>2</sub>O<sub>2</sub> on Pt/CeO<sub>2-x</sub>-R is the most favorable in the thermodynamics. The distinct dissociation processes strongly demonstrate the indispensable role of Pt, and favorable effects of the constructed nearby oxygen vacancies by hydrogen treatment. The corresponding configurations at various stages catalyzed by Pt/CeO<sub>2-x</sub>-R are also shown in Figure 4g, involving the electron transfer from TMB substrates to the nanozymes, the formation of oxTMB, and the proton transfer from the acidic reaction medium.<sup>[77]</sup> The remarkably enhanced catalytic efficiency can also be verified by the d-band center results. The calculated d-band center of Pt/CeO<sub>2-x</sub>-R is -2.59 eV (Figure 4i), which is closer to the Fermi level than that of Pt/CeO<sub>2</sub> counterparts (Figure 4h), indicating the stronger adsorption interaction of H<sub>2</sub>O<sub>2</sub> on the Pt/CeO<sub>2-x</sub>-R surfaces. These theoretical and experimental results clearly demonstrate that Pt/CeO<sub>2-x</sub>-R with rich and stable oxygen vacancies exhibit higher peroxidase-like performance due to the remarkable synergistic effect between Pt and oxygen vacancy, which can be potentially used as an effective catalytic therapy reagent for cancer therapy.

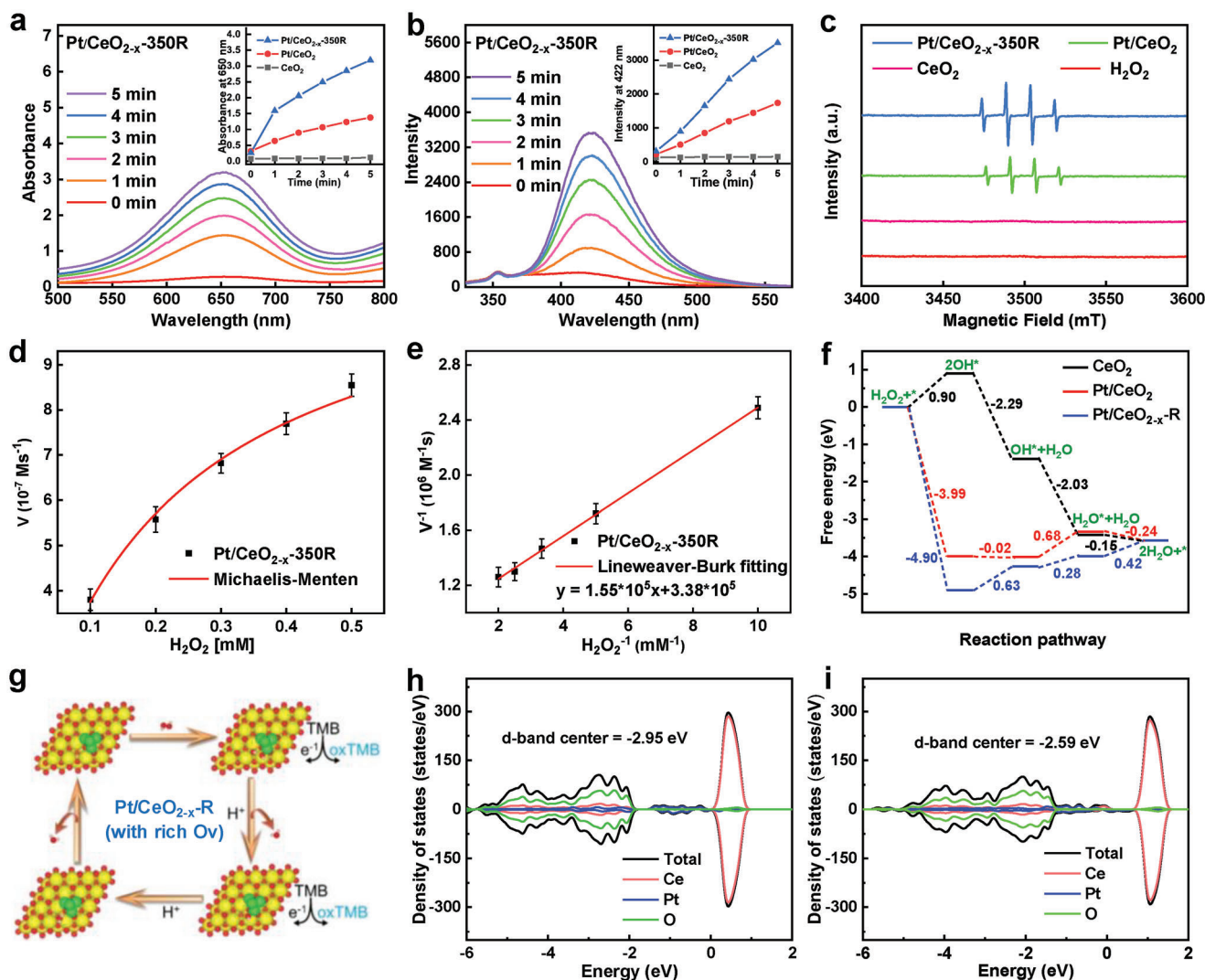


**Figure 4.** Identification of  $\cdot\text{OH}$  generation and DFT calculation results. a) UV-vis absorption spectra of TMB solution in tris-HCl buffer solution (pH 5.4) treated with  $\text{Pt/CeO}_{2-x}\text{-350R}$  in the presence of  $\text{H}_2\text{O}_2$ . (Inset is the relative UV-vis absorption intensity at 650 nm treated with  $\text{CeO}_2$ ,  $\text{Pt/CeO}_2$ , and  $\text{Pt/CeO}_{2-x}\text{-350R}$ .) b) Fluorescence spectra of TA in tris-HCl buffer solution (pH 5.4) oxidized by  $\cdot\text{OH}$  generated from the reactions between  $\text{Pt/CeO}_{2-x}\text{-350R}$  and  $\text{H}_2\text{O}_2$  (inset is the relative fluorescence intensity at 422 nm treated with  $\text{CeO}_2$ ,  $\text{Pt/CeO}_2$ , and  $\text{Pt/CeO}_{2-x}\text{-350R}$ .) c) EPR spectra of  $\text{CeO}_2$ ,  $\text{Pt/CeO}_2$ , and  $\text{Pt/CeO}_{2-x}\text{-350R}$  in coexistence with  $\text{H}_2\text{O}_2$  ( $\text{H}_2\text{O}_2$  alone is shown as control) in tris-HCl buffer solution (pH 5.4). d) Michaelis-Menten kinetics and e) Lineweaver-Burk plots of  $\text{Pt/CeO}_{2-x}\text{-350R}$  in coexistence with  $\text{H}_2\text{O}_2$  in tris-HCl buffer solution (pH 5.4). f) The free energy diagrams for the peroxidase (POD)-like catalysis mechanism on  $\text{CeO}_2$ ,  $\text{Pt/CeO}_2$ , and  $\text{Pt/CeO}_{2-x}\text{-R}$ . g) The catalytic mechanism along the POD-like reaction path over the  $\text{Pt/CeO}_{2-x}\text{-R}$ . The density of state (DOS) of the h)  $\text{Pt/CeO}_2$  and i)  $\text{Pt/CeO}_{2-x}\text{-R}$  and the corresponding  $d$  band centers of the elements.

### 2.3. PEG Modification

To enhance the stability and biocompatibility of  $\text{Pt/CeO}_{2-x}\text{-350R}$  under physiological environment, polyethylene glycol (PEG) was utilized to modify its surface. The confirmation of the modification of  $\text{Pt/CeO}_{2-x}\text{-350R}$  by PEG was achieved through the utilization of Fourier transform infrared (FTIR) spectroscopy. As shown in Figure S16a, Supporting Information, the spectra of  $\text{Pt/CeO}_{2-x}\text{-350R-PEG}$  showed three characteristic absorption peaks at 3411, 1384, and 1242  $\text{cm}^{-1}$ , which is attributed to the vibration of  $-\text{OH}$ ,  $\text{C}-\text{O}-\text{C}$ , and  $\text{Ce}-\text{O}$ , respectively, demonstrating the successful PEG modification on the surface of  $\text{Pt/CeO}_{2-x}\text{-350R}$ . The loading rate of PEG was calculated to be 42.13%

according to the thermogravimetric analysis (TGA) measurement (Figure S16b, Supporting Information). Using the dynamic light scattering (DLS) technique, the hydrodynamic sizes of  $\text{Pt/CeO}_{2-x}\text{-350R}$  and  $\text{Pt/CeO}_{2-x}\text{-350R-PEG}$  were determined to be around  $190.1 \pm 5.7$  and  $220.1 \pm 5.9$  nm (Figure S17a, Supporting Information), respectively. Importantly, the size of  $\text{Pt/CeO}_{2-x}\text{-350R-PEG}$  in different media (water, PBS, and high glucose Dulbecco's modified Eagles medium (DMEM)) was found to remain the same over a period of 2 weeks (Figure S17b, Supporting Information), thereby signifying their dispersion stability in the long term. In addition, the zeta potential value was also used to evaluate the stability of  $\text{Pt/CeO}_{2-x}\text{-350R}$  before and after the modification of PEG. As shown in Figure S17c,

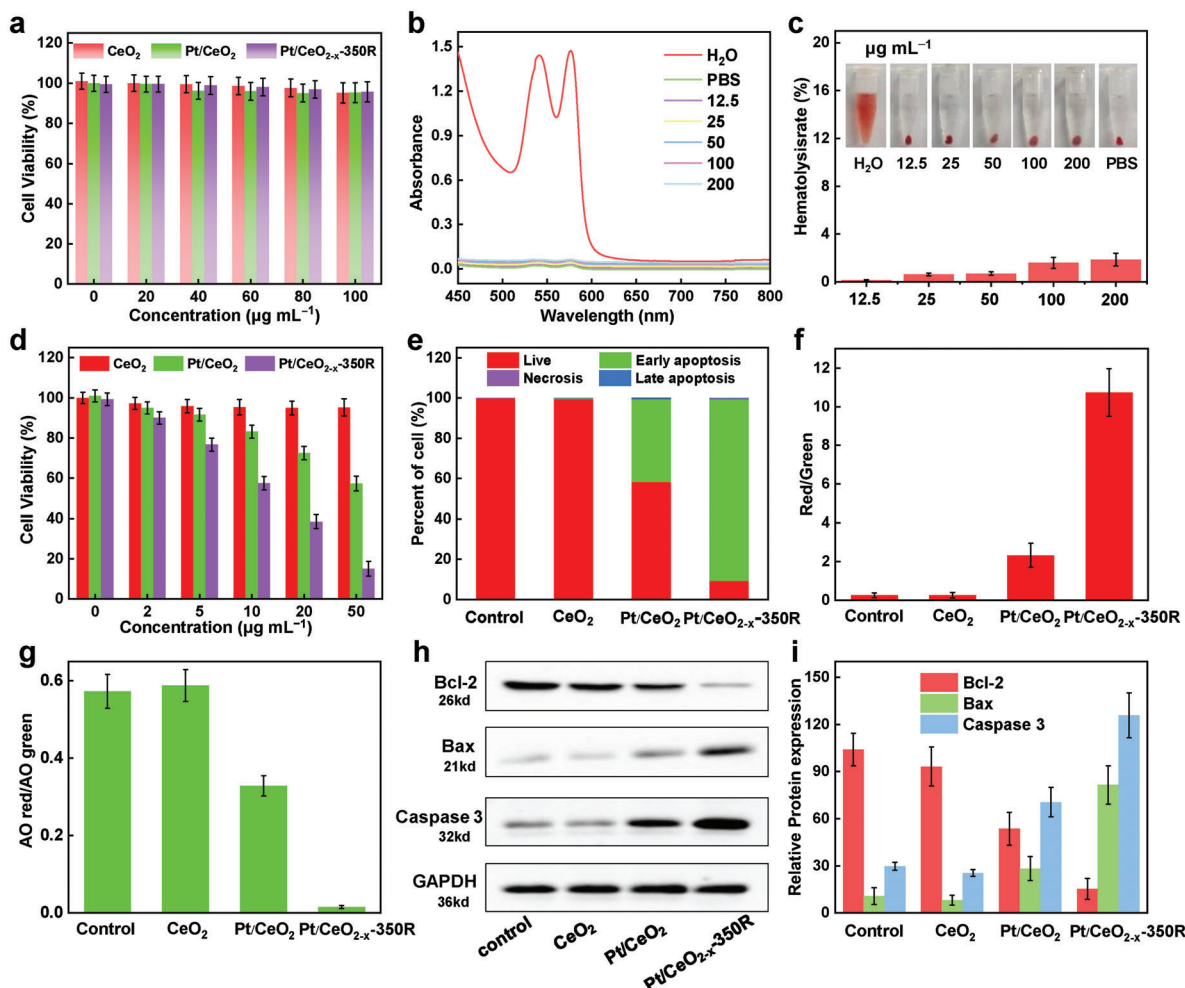


**Figure 5.** In vitro catalytic therapy effects on 4T1 cells. a) Cell viability of 4T1 cells incubated with various concentrations of CeO<sub>2</sub>-PEG, Pt/CeO<sub>2</sub>-PEG, and Pt/CeO<sub>2-x</sub>-350R-PEG. Data are presented as mean values  $\pm$  s.d. ( $n = 3$ ). b) The absorption spectra of the RBCs supernatant after being treated with H<sub>2</sub>O, PBS, and different concentrations of the Pt/CeO<sub>2-x</sub>-350R-PEG. c) Hemolysis rate of Pt/CeO<sub>2-x</sub>-350R-PEG at different concentrations. Inset: The photographs of the samples of H<sub>2</sub>O, Pt/CeO<sub>2-x</sub>-350R-PEG (12.5, 25, 50, 100, and 200  $\mu\text{g mL}^{-1}$ ), and PBS from left to right. Data are presented as mean values  $\pm$  s.d. ( $n = 3$ ). d) Cell viability of 4T1 cells after different treatments. Data are presented as mean values  $\pm$  s.d. ( $n = 3$ ). e) The quantitative apoptosis analysis of 4T1 cells handled with different formulations. f) Fluorescence intensity ratio of JC-1 red and green fluorescence of 4T1 cells after various treatments. Data are presented as mean values  $\pm$  s.d. ( $n = 3$ ). g) Fluorescence intensity ratio of AO red and AO green fluorescence of 4T1 cells after various treatments. Data are presented as mean values  $\pm$  s.d. ( $n = 3$ ). h) Western blot images and i) corresponding intensity of the expression of Bcl-2, Bax, and Caspase 3 proteins after different treatments.

Supporting Information, the zeta potential of Pt/CeO<sub>2-x</sub>-350R in water was measured to be  $-23.5 \pm 1.6$  mV, which is similar with that of Pt/CeO<sub>2-x</sub>-350R-PEG ( $-24.3 \pm 1.4$  mV). The zeta potentials of Pt/CeO<sub>2-x</sub>-350R-PEG in PBS and DMEM were close to those in water (Figure S17c, Supporting Information), suggesting that PEG can enhance the stability and biocompatibility of Pt/CeO<sub>2-x</sub>-350R under the physiological environment, which will be beneficial for the subsequent SDT treatment.

## 2.4. In Vitro Catalytic Therapy Studies Performed on 4T1 Cells

Encouraged by the above exciting results, we further evaluated the  $\cdot\text{OH}$  production performance of Pt/CeO<sub>2-x</sub>-350R-PEG in vitro. First, the cytotoxicity of CeO<sub>2</sub>-PEG, Pt/CeO<sub>2</sub>-PEG and

Pt/CeO<sub>2-x</sub>-350R-PEG was assessed with 4T1 cells by the classical methyl thiazolyl tetrazolium (MTT) assay. As shown in Figure 5a, the cell survival rates were all above 95%, even at concentration up to 100  $\mu\text{g mL}^{-1}$ , demonstrating that all materials exhibited excellent biocompatibility. In Figure S18, Supporting Information, H<sub>2</sub>O<sub>2</sub> alone displayed negligible cytotoxicity even at the concentration of 1 mM. The hemolysis rate of Pt/CeO<sub>2-x</sub>-350R-PEG was detected to verify its biocompatibility. It was found that the hemolysis rates of Pt/CeO<sub>2-x</sub>-350R-PEG with different concentrations are all less than 2% (Figure 5b,c), indicating that Pt/CeO<sub>2-x</sub>-350R-PEG are safe to be used in vivo. Since sufficient intracellular accumulation of nanomaterials is a prerequisite for effective treatment, the cellular uptake of Pt/CeO<sub>2-x</sub>-350R-PEG was studied on 4T1 cells. In Figure S19, Supporting Information, the intense red

fluorescence signal from Rhodamine B (RhB)-labeled Pt/CeO<sub>2-x</sub>-350R-PEG was found in the cells at 8 h, indicating the effective cellular uptake of Pt/CeO<sub>2-x</sub>-350R-PEG. After confirming the biocompatibility and effective cell uptake of Pt/CeO<sub>2-x</sub>-350R-PEG, the in vitro therapeutic effects were assessed by MTT assay. As shown in Figure 5d, CeO<sub>2</sub>-PEG group did not display any cytotoxicity, while Pt/CeO<sub>2</sub>-PEG and Pt/CeO<sub>2-x</sub>-350R-PEG groups exhibited significant dose-dependent cytotoxicity. Compared with Pt/CeO<sub>2</sub>-PEG, the cell killing effect of Pt/CeO<sub>2-x</sub>-350R-PEG was remarkably enhanced, and the cell survival rate was only 15% at 50 µg mL<sup>-1</sup>, which was attributed to the excellent catalytic performance of Pt/CeO<sub>2-x</sub>-350R-PEG. Subsequently, the effectiveness of catalytic therapy was verified with calcein acetoxymethyl ester and propidium iodide (Calcein-AM/PI, Figure S20, Supporting Information). Clearly, the cells in the DMEM or CeO<sub>2</sub>-PEG group showed intense green fluorescence, implying ignorable cell damage. Comparatively, there were obvious dead cells in Pt/CeO<sub>2</sub>-PEG and Pt/CeO<sub>2-x</sub>-350R-PEG groups as red fluorescence could be observed. Particularly, the number of dead cells in Pt/CeO<sub>2-x</sub>-350R-PEG group was significantly higher than that in Pt/CeO<sub>2</sub>-PEG group, which was consistent with the results of MTT assay. To further explore the mechanism of Pt/CeO<sub>2-x</sub>-350R-PEG-induced cell death, a fluorescent probe 2',7'-dichlorofluorescein diacetate (DCFH-DA) was chosen to assess the intracellular ·OH production. In Figure S21, Supporting Information, the strong green fluorescence signal was observed in cells treated with Pt/CeO<sub>2-x</sub>-350R-PEG, while the weak fluorescence was emitted in the control, CeO<sub>2</sub>-PEG, and Pt/CeO<sub>2</sub>-PEG groups, suggesting that Pt/CeO<sub>2-x</sub>-350R-PEG could induce cell death by generating ·OH. Additionally, apoptosis assay was conducted by flow cytometry with Annexin V-fluorescein isothiocyanate (Annexin V-FITC)/PI fluorescence probe. The results demonstrated that Pt/CeO<sub>2-x</sub>-350R-PEG induced the most significantly catalytic therapy-related cell apoptosis, and the apoptosis rate was up to 90.63% (Figure 5e; Figure S22, Supporting Information).

Mitochondria are important organelles related to cellular energy conversion and apoptosis, which are susceptible to damage by ROS, resulting in the change of mitochondrial membrane potential (MMP). Therefore, the 5,5',6,6'-tetrachloro-1,1'-3,3'-tetraethyl-benzimidazolylcarbocyanine iodide (JC-1) probe was applied to directly reflect ROS-induced mitochondrial dysfunction. Compared with control and CeO<sub>2</sub>-PEG groups, Pt/CeO<sub>2</sub>-PEG or Pt/CeO<sub>2-x</sub>-350R-PEG treated cells exhibited the higher ratio of Red/Green (R/G) fluorescence intensity. Particularly, Pt/CeO<sub>2-x</sub>-350R-PEG led to the greatest R/G increase for 4T1 cells, owing to the production of ·OH and significant mitochondrial dysfunction (Figure 5f; Figure S23, Supporting Information). Then, acridine orange (AO) probe was further used to monitor the lysosome destruction of 4T1 cells. As shown in Figure 5g and Figure S24, Supporting Information, the Pt/CeO<sub>2-x</sub>-350R-PEG group displayed strong green fluorescence signal in the whole cytoplasm, and the red fluorescence signal nearly disappeared, indicating severe oxidative injury to 4T1 cells. Based on the above results, we further investigated the cytotoxicity mechanism by Western blot. As shown in Figure 5h,i, Bax and Caspase 3 proteins were significantly increased and Bcl-2 protein was decreased in cells treated with Pt/CeO<sub>2</sub>-PEG and Pt/CeO<sub>2-x</sub>-350R-PEG compared with cells treated with CeO<sub>2</sub>-PEG. Noticeably, the

expression of Bax and Caspase 3 proteins was the highest, while the Bcl-2 protein was the lowest when cells were treated with Pt/CeO<sub>2-x</sub>-350R-PEG, which is ascribed to the superior enzyme-like catalytic therapeutic efficacy.

## 2.5. In Vivo Catalytic Therapy Treatment

Inspired by the excellent in vitro catalytic therapy results, we were encouraged to carry out a series of animal experiments to further evaluate the therapeutic efficiency in vivo. First, the biodistribution of Pt/CeO<sub>2-x</sub>-350R-PEG was studied in vivo. After intravenous injection of Pt/CeO<sub>2-x</sub>-350R-PEG, the main organs and tumors of mice were collected at different time points and the Ce level was tested by inductively coupled plasma-atomic emission spectrometry (ICP-AES). As expected, the Pt/CeO<sub>2-x</sub>-350R-PEG was significantly accumulated at tumor and reached the maximum accumulation at 8 h post-injection (Figure 6a). Moreover, the pharmacokinetics analysis of the Pt/CeO<sub>2-x</sub>-350R-PEG was conducted by measuring the concentration of Ce in blood at different time points post-injection, and the blood circulation half-life is 0.22 h (*t*<sub>1/2(α)</sub>) and 7.52 h (*t*<sub>1/2(β)</sub>), presenting a two-compartment model. The long blood circulation time confirmed that Pt/CeO<sub>2-x</sub>-350R-PEG could effectively accumulate at the tumor site (Figure 6b). The clearance rate of Pt/CeO<sub>2-x</sub>-350R-PEG was calculated to be 0.0129 L/h.<sup>[78]</sup> When the tumor volume reached 80 mm<sup>3</sup>, the mice were divided randomly and treated with PBS, CeO<sub>2</sub>-PEG, Pt/CeO<sub>2</sub>-PEG, and Pt/CeO<sub>2-x</sub>-350R-PEG, respectively. The tumor volume of each mouse was monitored every 2 days. As shown in Figure 6c,d, rapid tumor growth appeared in mice treated with PBS and CeO<sub>2</sub>-PEG, while the tumor growth of mice treated with Pt/CeO<sub>2</sub>-PEG was moderately inhibited. Excitingly, the tumors in Pt/CeO<sub>2-x</sub>-350R-PEG group were significantly ablated without recurrence during the treatment period, suggesting the excellent anti-tumor efficacy of Pt/CeO<sub>2-x</sub>-350R-PEG. The representative photos of corresponding mice also confirmed the above results (Figure 6e; Figure S25, Supporting Information). After 16 days of treatment, all the mice were sacrificed, and tumor tissues were collected. Average tumor weight and the representative photos of corresponding tumors confirmed the excellent therapeutic effect of Pt/CeO<sub>2-x</sub>-350R-PEG (Figure 6f; Figure S26, Supporting Information). To quantitatively verify the nanozyme-catalyzed therapeutic efficiency responsible for anti-neoplastic performance, the tumor growth inhibition (TGI) rate was calculated (Figure 6g). Interestingly, Pt/CeO<sub>2-x</sub>-350R-PEG caused the highest tumor inhibition ratios of 94.49% on 4T1 tumor-bearing mice, which was evidently higher than that of the Pt/CeO<sub>2</sub>-PEG (53.88%) and CeO<sub>2</sub>-PEG groups (3.86%).

In addition, the survival time of each 4T1 tumor-bearing nude mouse in all groups was also recorded to evaluate the therapeutic effect in vivo. Benefiting from the outstanding therapeutic performance, the survival rate of mice administrated with Pt/CeO<sub>2-x</sub>-350R-PEG was much longer than those treated with PBS, CeO<sub>2</sub>-PEG, and Pt/CeO<sub>2</sub>-PEG (Figure 6h). As shown in Figure S27, Supporting Information, there was no obvious body weight change in all mice during the experiment period, which indicates the negligible side effects of materials. Furthermore, H&E staining experiments were performed to assess the cellular damage degree and necrosis level. In Figure S28,

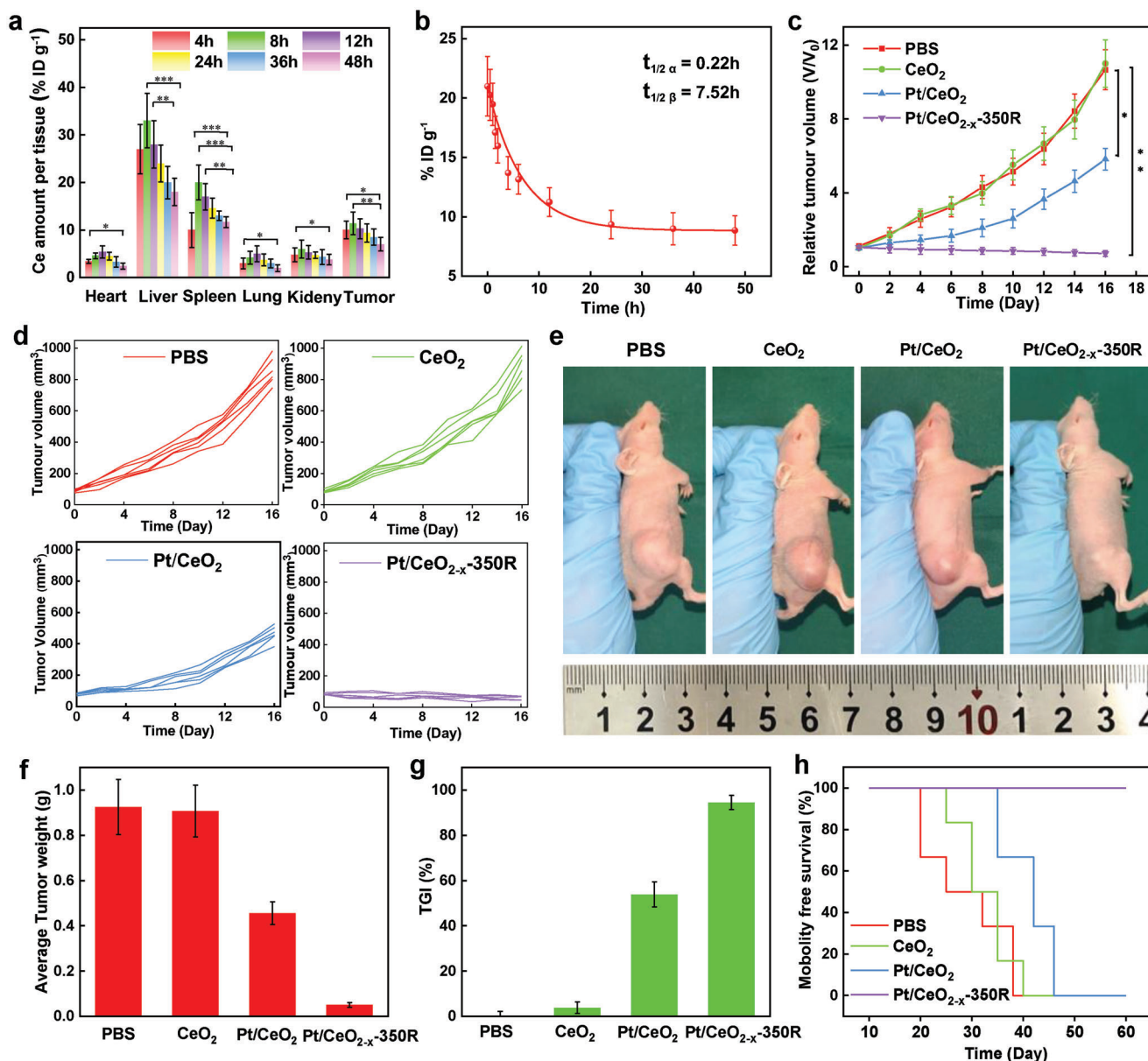


**Figure 6.** In vivo catalytic therapy effects of Pt/CeO<sub>2-x</sub>-350R-PEG conducted on 4T1 tumor-bearing mice. a) Biodistribution of Pt/CeO<sub>2-x</sub>-350R-PEG in main organs and tumors after intravenous injection for 4, 8, 12, 24, 36, and 48 h. Data are presented as mean values  $\pm$  s.d. ( $n = 3$ ). b) Blood circulation curve of Pt/CeO<sub>2-x</sub>-350R-PEG determined by Ce concentration in the blood of mice at different time points post-injection. Data are presented as mean values  $\pm$  s.d. ( $n = 3$ ). c) Relative tumor volumes and d) individual tumor growth curves of 4T1 tumor-bearing mice after various treatments. Data are presented as mean values  $\pm$  s.d. ( $n = 6$ ). e) Representative photos and f) average tumor weight of 4T1 tumor-bearing mice with different treatments for 16 days. Data are presented as mean values  $\pm$  s.d. ( $n = 6$ ). g) Tumor inhibition rates of 4T1 tumor-bearing mice after different treatments. Data are presented as mean values  $\pm$  s.d. ( $n = 6$ ). h) Survival rates of 4T1 tumor-bearing mice after different treatments. One-way ANOVA was used to analyze statistical differences:  $*p < 0.05$ ,  $**p < 0.01$ ,  $***p < 0.001$ .

Supporting Information, compared with PBS, CeO<sub>2</sub>-PEG, and Pt/CeO<sub>2</sub>-PEG, Pt/CeO<sub>2</sub>-350R-PEG induced nuclear shrinkage and fragmentation to the largest extent. Similar results were also observed in the Ki-67 (Figure S29a, Supporting Information) and terminal deoxynucleotidyl transferase (TdT)-mediated deoxyuridine triphosphate (dUTP) nick-end labeling (TUNEL) staining images (Figures S29b and S30a, Supporting Information). Pt/CeO<sub>2-x</sub>-350R-PEG treatment also resulted in higher

level of apoptotic protein Caspase 3, and a large apoptosis area was seen in tumor section (Figures S29c and S30b, Supporting Information). Moreover, the excellent antitumor efficacy of Pt/CeO<sub>2-x</sub>-350R-PEG-mediated catalytic therapy is further validated by dihydroethidium (DHE) staining. As shown in Figures S29d and S30c, Supporting Information, remarkable red fluorescence of DHE could be found in Pt/CeO<sub>2</sub>-350R-PEG group, confirming a high level of ROS generation.

Furthermore, a series of biosafety experiments were performed. After intravenous injection of Pt/CeO<sub>2-x</sub>-350R-PEG, no apparent tissue damage was observed in major organs including the heart, liver, lung, spleen, and kidney (Figure S31, Supporting Information), demonstrating its excellent biosecurity. To further evaluate the biocompatibility and immune response of Pt/CeO<sub>2-x</sub>-350R-PEG, the blood routine examinations were carried out to measure the levels of the relative indexes after 1 and 16 days post-injection. Figure S32, Supporting Information, exhibits that the levels of the relative indexes (such as alanine aminotransferase (ALT), aspartate aminotransferase (AST), blood urea (UREA), creatinine (CREA), white blood cell count (WBC), hemoglobin (HGB), platelet count (PLT)) in mice treated with Pt/CeO<sub>2-x</sub>-350R-PEG were as similar as those in control group, suggesting that there was no evident infection or inflammation caused by Pt/CeO<sub>2-x</sub>-350R-PEG. We also investigated the excretion of Pt/CeO<sub>2-x</sub>-350R-PEG in mice. In Figure S33, Supporting Information, Pt/CeO<sub>2-x</sub>-350R-PEG could be excreted via feces and urine, strengthening its application as nanozyme for catalytic therapy.

### 3. Conclusion

In summary, we have successfully realized the regulation of oxygen vacancies and electronic structure of Pt via reduction of CeO<sub>2</sub> NRs supported Pt nanoclusters/SAs by H<sub>2</sub> gas under mild temperature (350 °C) to prepare Pt/CeO<sub>2-x</sub>-350R as a highly active nanozyme for catalytic therapy. The ALD-deposited Pt nanoclusters/SAs onto CeO<sub>2</sub> not only facilitate the production of oxygen vacancies through the hydrogen spillover effect during the reduction process but also stabilize the resulting oxygen vacancies. Simultaneously, the oxygen vacancies provide binding sites for Pt nanoclusters to establish strong metal-support interactions, thereby preventing their coalescence and enhancing their catalytic activity. Importantly, the Pt/CeO<sub>2-x</sub>-350R exhibited superior catalytic activity for ROS generation, outperforming the as prepared CeO<sub>2</sub> NRs ( $\approx 27.4$  times) and Pt/CeO<sub>2</sub> ( $\approx 2.3$  times). The remarkable enzyme-mimic catalytic performance of Pt/CeO<sub>2-x</sub>-350R can be attributed to the superior catalytic properties of defect-rich CeO<sub>2-x</sub> and Pt nanoclusters. After PEG modification, the Pt/CeO<sub>2-x</sub>-350R presented the excellent performance to produce toxic ROS in the TEM, thereby triggering cell death in vitro and tumor ablation in vivo. Our study provides a promising approach for design of nanozymes with exceptional performance based on metal oxide/noble metal nanocomposites. We believe that the strategy of stable and synergistic interaction between metal and oxygen vacancies is also suitable for tuning metal oxides for other cancer therapeutic strategies, such as sonodynamic therapy, photothermal therapy, and radiation therapy.

### Supporting Information

Supporting Information is available from the Wiley Online Library or from the author.

### Acknowledgements

J.Z., Y.Y., and F.Q. contributed equally to this work. All animal experiments were permitted by the Animal Care and Use Committee of China-

Japan Friendship Hospital. All study procedures were performed in accordance with the protocols approved by the Animal Research Center of China-Japan Friendship Hospital. The authors appreciate the financial support from the National Natural Science Foundation of China (22102131, U1910209), National Science Fund for Distinguished Young Scholars (21825204), Fundamental Research Funds for the Central Universities (G2023KY0605), and Natural Science Basic Research Plan in Shaanxi Province of China (2021JQ-090). Z.Z. thanks the funding support from National Natural Science Foundation of China (52102348) and the Science and Technology Innovation Talent Program of University in Henan Province (23HASTIT016). C.T. thanks the funding support from the National Natural Science Foundation of China-Excellent Young Scientists Fund (Hong Kong and Macau) (52122002). R.L. thanks the funding support from National Natural Science Foundation of China (22288102, 21971007) and the Beijing Natural Science Foundation (2212044). The authors would like to thank the Analytical & Testing Center of Northwestern Polytechnical University for HAADF-STEM measurements and Shanghai Synchrotron Radiation Facility for XAFS measurements. Dr. Fangxian Cao is acknowledged for guiding the synthesis of porous CeO<sub>2</sub> NRs.

### Conflict of Interest

The authors declare no conflict of interest.

### Data Availability Statement

The data that support the findings of this study are available from the corresponding author upon reasonable request.

### Keywords

catalytic therapy, CeO<sub>2</sub> nanomaterials, nanozymes, oxygen vacancies, Pt nanoclusters

Received: June 30, 2023

Revised: August 9, 2023

Published online: September 22, 2023

- [1] S. Ji, B. Jiang, H. Hao, Y. Chen, J. Dong, Y. Mao, Z. Zhang, R. Gao, W. Chen, R. Zhang, Q. Liang, H. Li, S. Liu, Y. Wang, Q. Zhang, L. Gu, D. Duan, M. Liang, D. Wang, X. Yan, Y. Li, *Nat. Catal.* **2021**, 4, 407.
- [2] L. Jiao, H. Yan, Y. Wu, W. Gu, C. Zhu, D. Du, Y. Lin, *Angew. Chem., Int. Ed.* **2020**, 132, 2585.
- [3] J. Wu, Y. Yu, Y. Cheng, C. Cheng, Y. Zhang, B. Jiang, X. Zhao, L. Miao, H. Wei, *Angew. Chem., Int. Ed.* **2021**, 133, 1247.
- [4] J. Yang, H. Yao, Y. Guo, B. Yang, J. Shi, *Angew. Chem., Int. Ed.* **2022**, 134, e202200480.
- [5] J. Zhou, D. Xu, G. Tian, Q. He, X. Zhang, J. Liao, L. Mei, L. Chen, L. Gao, L. Zhao, G. Yang, W. Yin, G. Nie, Y. Zhao, *J. Am. Chem. Soc.* **2023**, 145, 4279.
- [6] Y. Zhu, P. Gong, J. Wang, J. Cheng, W. Wang, H. Cai, R. Ao, H. Huang, M. Yu, L. Lin, X. Chen, *Angew. Chem., Int. Ed.* **2023**, 135, e202218407.
- [7] W. Fu, X. Zhang, L. Mei, R. Zhou, W. Yin, Q. Wang, Z. Gu, Y. Zhao, *ACS Nano* **2020**, 14, 10001.
- [8] T. Hu, B. Xue, F. Meng, L. Ma, Y. Du, S. Yu, R. Ye, H. Li, Q. Zhang, L. Gu, Z. Zhou, R. Liang, C. Tan, *Adv. Healthcare Mater.* **2023**, 12, 2202911.
- [9] S. Sun, Q. Chen, Y. Li, Y. Yu, Z. Li, H. Lin, *SmartMat* **2022**, 3, 311.
- [10] H. Chen, X. He, Z. Zhou, Z. Wu, H. Li, X. Peng, Y. Zhou, C. Tan, J. Shen, *J. Nanobiotechnol.* **2022**, 20, 136.

- [11] Y. Li, L. Huang, T. Du, L. Shi, S. Liu, J. Sun, D. Zhang, J. Wang, *Sci. Bull.* **2023**, 68, 441.
- [12] Y. Huang, J. Ren, X. Qu, *Chem. Rev.* **2019**, 119, 4357.
- [13] Y. Ai, Z.-N. Hu, X. Liang, H.-B. Sun, H. Xin, Q. Liang, *Adv. Funct. Mater.* **2022**, 32, 2110432.
- [14] B. Yang, Y. Chen, J. Shi, *Adv. Mater.* **2019**, 31, 1901778.
- [15] R. Yan, S. Sun, J. Yang, W. Long, J. Wang, X. Mu, Q. Li, W. Hao, S. Zhang, H. Liu, Y. Gao, L. Ouyang, J. Chen, S. Liu, X.-D. Zhang, D. Ming, *ACS Nano* **2019**, 13, 11552.
- [16] Z. Wang, Y. Zhao, Y. Hou, G. Tang, R. Zhang, Y. Yang, X. Yan, K. Fan, *Adv. Mater.* **2023**, 35, 202210144.
- [17] W. Gao, J. He, L. Chen, X. Meng, Y. Ma, L. Cheng, K. Tu, X. Gao, C. Liu, M. Zhang, K. Fan, D.-W. Pang, X. Yan, *Nat. Commun.* **2023**, 14, 160.
- [18] Q. Li, T. Wu, O. U. Akakuru, N. Song, W. Liu, W. Jiang, K. Fan, *Adv. Funct. Mater.* **2023**, 33, 2214826.
- [19] J. Guo, X. Qin, K. Ye, H. Wang, P. Li, T. Chen, L. Ma, H. Lin, *Surf. Interfaces* **2023**, 40, 103083.
- [20] L. Gao, J. Zhuang, L. Nie, J. Zhang, Y. Zhang, N. Gu, T. Wang, J. Feng, D. Yang, S. Perrett, X. Yan, *Nat. Nanotechnol.* **2007**, 2, 577.
- [21] Y. Yang, T. Hu, Y. Bian, F. Meng, S. Yu, H. Li, Q. Zhang, L. Gu, X. Weng, C. Tan, R. Liang, *Adv. Mater.* **2023**, 35, 2211205.
- [22] Z. Lv, T. Hu, Y. Bian, G. Wang, Z. Wu, H. Li, X. Liu, S. Yang, C. Tan, R. Liang, X. Weng, *Adv. Mater.* **2023**, 35, 2206545.
- [23] T. Hu, Z. Gu, G. R. Williams, M. Strimaite, J. Zha, Z. Zhou, X. Zhang, C. Tan, R. Liang, *Chem. Soc. Rev.* **2022**, 51, 6126.
- [24] M. Liang, X. Yan, *Acc. Chem. Res.* **2019**, 52, 2190.
- [25] J. Sheng, Y. Wu, H. Ding, K. Feng, Y. Shen, Y. Zhang, N. Gu, *Adv. Mater.* **2023**, 2211210, <https://doi.org/10.1002/adma.202211210>.
- [26] Y. Chen, Q. Tian, H. Wang, R. Ma, R. Han, Y. Wang, H. Ge, Y. Ren, R. Yang, H. Yang, Y. Chen, X. Duan, L. Zhang, J. Gao, L. Gao, X. Yan, Y. Qin, *Adv. Mater.* **2022**, 2206421, <https://doi.org/10.1002/adma.202206421>.
- [27] L. Huang, J. Chen, L. Gan, J. Wang, S. Dong, *Sci. Adv.* **2019**, 5, eaav5490.
- [28] F. Gao, T. Shao, Y. Yu, Y. Xiong, L. Yang, *Nat. Commun.* **2021**, 12, 745.
- [29] S. Zhao, H. Li, R. Liu, N. Tao, L. Deng, Q. Xu, J. Hou, J. Sheng, J. Zheng, L. Wang, W. Chen, S. Guo, Y.-N. Liu, *J. Am. Chem. Soc.* **2023**, 145, 10322.
- [30] R. Zhang, B. Xue, Y. Tao, H. Zhao, Z. Zhang, X. Wang, X. Zhou, B. Jiang, Z. Yang, X. Yan, K. Fan, *Adv. Mater.* **2022**, 34, 2205324.
- [31] J. Yang, R. Zhang, H. Zhao, H. Qi, J. Li, J. Li, X. Zhou, A. Wang, K. Fan, X. Yan, T. Zhang, *Exploration* **2022**, 2, 20210267.
- [32] X. Meng, D. Li, L. Chen, H. He, Q. Wang, C. Hong, J. He, X. Gao, Y. Yang, B. Jiang, G. Nie, X. Yan, L. Gao, K. Fan, *ACS Nano* **2021**, 15, 5735.
- [33] X. Zhao, H. Qiu, Y. Shao, P. Wang, S. Yu, H. Li, Y. Zhou, Z. Zhou, L. Ma, C. Tan, *Acta Phys.-Chim. Sin.* **2023**, 39, 2211043.
- [34] B. Xue, X. Geng, H. Cui, H. Chen, Z. Wu, H. Chen, H. Li, Z. Zhou, M. Zhao, C. Tan, J. Li, *Chin. Chem. Lett.* **2023**, 34, 108140.
- [35] H. Zhou, Y. Wu, *Sci. Bull.* **2023**, 68, 465.
- [36] H. Zhang, Y. Chen, W. Hua, W. Gu, H. Zhuang, H. Li, X. Jiang, Y. Mao, Y. Liu, D. Jin, W. Bu, *Angew. Chem., Int. Ed.* **2023**, 62, e202300356.
- [37] H. Wu, F. Xia, L. Zhang, C. Fang, J. Lee, L. Gong, J. Gao, D. Ling, F. Li, *Adv. Mater.* **2022**, 34, 2108348.
- [38] A. Yuan, F. Xia, Q. Bian, H. Wu, Y. Gu, T. Wang, R. Wang, L. Huang, Q. Huang, Y. Rao, D. Ling, F. Li, J. Gao, *ACS Nano* **2021**, 15, 13759.
- [39] W. Ji, Y. Li, H. Peng, R. Zhao, J. Shen, Y. Wu, J. Wang, Q. Hao, Z. Lu, J. Yang, X. Zhang, *Adv. Mater.* **2022**, 34, 2105711.
- [40] F. Muhammad, F. Huang, Y. Cheng, X. Chen, Q. Wang, C. Zhu, Y. Zhang, X. Yang, P. Wang, H. Wei, *ACS Nano* **2022**, 16, 20567.
- [41] Y. Chen, Y. Liu, C. Guo, C. Yin, C. Xie, Q. Fan, *Adv. Funct. Mater.* **2023**, 33, 2209927.
- [42] Y. Ma, Z. Tian, W. Zhai, Y. Qu, *Nano Res.* **2022**, 15, 10328.
- [43] Y. Chen, S. Ji, W. Sun, Y. Lei, Q. Wang, A. Li, W. Chen, G. Zhou, Z. Zhang, Y. Wang, L. Zheng, Q. Zhang, L. Gu, X. Han, D. Wang, Y. Li, *Angew. Chem., Int. Ed.* **2020**, 132, 1311.
- [44] J. Zhang, Z. Gao, S. Wang, G. Wang, X. Gao, B. Zhang, S. Xing, S. Zhao, Y. Qin, *Nat. Commun.* **2019**, 10, 4166.
- [45] Y. Wu, W. Xu, L. Jiao, Y. Tang, Y. Chen, W. Gu, C. Zhu, *Mater. Today* **2022**, 52, 327.
- [46] S. Chu, C. Kang, W. Park, Y. Han, S. Hong, L. Hao, H. Zhang, T. W. B. Lo, A. W. Robertson, Y. Jung, B. Han, Z. Sun, *SmartMat* **2022**, 3, 194.
- [47] Y. Chen, C. Chen, X. Cao, Z. Wang, N. Zhang, T. Liu, *Acta Phys.-Chim. Sin.* **2023**, 39, 2212053.
- [48] Y. Wan, F. Fang, R. Sun, J. Zhang, K. Chang, *Acta Phys.-Chim. Sin.* **2023**, 39, 2212042.
- [49] X. Li, X. Zhao, D. Chu, X. Zhu, B. Xue, H. Chen, Z. Zhou, J. Li, *Surf. Interfaces* **2022**, 33, 102247.
- [50] Z. Zhou, T. Wang, T. Hu, C. Cheng, S. Yu, H. Li, S. Liu, L. Ma, M. Zhao, R. Liang, C. Tan, *Mater. Chem. Front.* **2023**, 7, 1684.
- [51] Z. Zhou, X. Li, T. Hu, B. Xue, H. Chen, L. Ma, R. Liang, C. Tan, *Adv. Nanobiomed. Res.* **2022**, 2, 2200065.
- [52] W. Shen, T. Hu, X. Liu, J. Zha, F. Meng, Z. Wu, Z. Cui, Y. Yang, H. Li, Q. Zhang, L. Gu, R. Liang, C. Tan, *Nat. Commun.* **2022**, 13, 3384.
- [53] T. Hu, W. Shen, F. Meng, S. Yang, S. Yu, H. Li, Q. Zhang, L. Gu, C. Tan, R. Liang, *Adv. Mater.* **2023**, 35, 2209692.
- [54] B. Yu, W. Wang, W. Sun, C. Jiang, L. Lu, *J. Am. Chem. Soc.* **2021**, 143, 8855.
- [55] Z. Zhou, Y. Wang, F. Peng, F. Meng, J. Zha, L. Ma, Y. Du, N. Peng, L. Ma, Q. Zhang, L. Gu, W. Yin, Z. Gu, C. Tan, *Angew. Chem., Int. Ed.* **2022**, 61, e202115939.
- [56] S. Dong, Y. Dong, B. Liu, J. Liu, S. Liu, Z. Zhao, W. Li, B. Tian, R. Zhao, F. He, S. Gai, Y. Xie, P. Yang, Y. Zhao, *Adv. Mater.* **2022**, 34, 2107054.
- [57] S. Dong, Y. Dong, Z. Zhao, J. Liu, S. Liu, L. Feng, F. He, S. Gai, Y. Xie, P. Yang, *J. Am. Chem. Soc.* **2023**, 145, 9488.
- [58] M. Si, Z. Lin, Z. Chen, X. Sun, H. Wang, P. D. Ye, *Nat. Electron.* **2022**, 5, 164.
- [59] B. Gupta, M. Hossain, A. Riaz, A. Sharma, D. Zhang, H. H. Tan, C. Jagadish, K. Catchpole, B. Hoex, S. Karuturi, *Adv. Funct. Mater.* **2022**, 32, 2109105.
- [60] S. Zhang, C.-R. Chang, Z.-Q. Huang, J. Li, Z. Wu, Y. Ma, Z. Zhang, Y. Wang, Y. Qu, *J. Am. Chem. Soc.* **2016**, 138, 2629.
- [61] K. Zhang, Q. Meng, H. Wu, J. Yan, X. Mei, P. An, L. Zheng, J. Zhang, M. He, B. Han, *J. Am. Chem. Soc.* **2022**, 144, 20834.
- [62] Y. Chen, J. Lin, L. Li, B. Qiao, J. Liu, Y. Su, X. Wang, *ACS Catal.* **2018**, 8, 859.
- [63] S. Xie, L. Liu, Y. Lu, C. Wang, S. Cao, W. Diao, J. Deng, W. Tan, L. Ma, S. N. Ehrlich, Y. Li, Y. Zhang, K. Ye, H. Xin, M. Flytzani-Stephanopoulos, F. Liu, *J. Am. Chem. Soc.* **2022**, 144, 21255.
- [64] B. Song, D. Choi, Y. Xin, C. R. Bowers, H. Hagelin-Weaver, *Angew. Chem., Int. Ed.* **2021**, 60, 4038.
- [65] J. Ke, W. Zhu, Y. Jiang, R. Si, Y.-J. Wang, S.-C. Li, C. Jin, H. Liu, W.-G. Song, C.-H. Yan, Y.-W. Zhang, *ACS Catal.* **2015**, 5, 5164.
- [66] W. Tan, S. Xie, D. Le, W. Diao, M. Wang, K.-B. Low, D. Austin, S. Hong, F. Gao, L. Dong, L. Ma, S. N. Ehrlich, T. S. Rahman, F. Liu, *Nat. Commun.* **2022**, 13, 7070.
- [67] J. Lee, Y. Ryou, X. Chan, T. J. Kim, D. H. Kim, *J. Phys. Chem. C* **2016**, 120, 25870.
- [68] X. Wei, X. Wen, Y. Liu, C. Chen, C. Xie, D. Wang, M. Qiu, N. He, P. Zhou, W. Chen, J. Cheng, H. Lin, J. Jia, X.-Z. Fu, S. Wang, *J. Am. Chem. Soc.* **2022**, 144, 11530.
- [69] L. Wang, Y. Yu, H. He, Y. Zhang, X. Qin, B. Wang, *Sci. Rep.* **2017**, 7, 12845.

- [70] M. Chen, X. Zhou, C. Xiong, T. Yuan, W. Wang, Y. Zhao, Z. Xue, W. Guo, Q. Wang, H. Wang, Y. Li, H. Zhou, Y. Wu, *ACS Appl. Mater. Interfaces* **2022**, *14*, 21989.
- [71] H. Yan, N. Zhang, D. Wang, *Chem Catal.* **2022**, *2*, 1594.
- [72] M. Xiong, Z. Gao, Y. Qin, *ACS Catal.* **2021**, 3159.
- [73] R. Prins, *Chem. Rev.* **2012**, *112*, 2714.
- [74] C. T. Campbell, C. H. F. Peden, *Science* **2005**, *309*, 713.
- [75] Z. Xi, K. Wei, Q. Wang, M. J. Kim, S. Sun, V. Fung, X. Xia, *J. Am. Chem. Soc.* **2021**, *143*, 2660.
- [76] X. Shen, Z. Wang, X. J. Gao, X. Gao, *Adv. Mater.* **2023**, 2211151, <https://doi.org/10.1002/adma.202211151>.
- [77] Y. Wang, G. Jia, X. Cui, X. Zhao, Q. Zhang, L. Gu, L. Zheng, L. H. Li, Q. Wu, D. J. Singh, D. Matsumura, T. Tsuji, Y. Cui, J. Zhao, W. Zheng, *Chem* **2021**, *7*, 436.
- [78] J. Zou, J. Zhu, Z. Yang, L. Li, W. Fan, L. He, W. Tang, L. Deng, J. Mu, Y. Ma, Y. Cheng, W. Huang, X. Dong, X. Chen, *Angew. Chem., Int. Ed.* **2020**, *59*, 8833.